TISSUE REGENERATION

Skeletal muscle regeneration with robotic actuation–mediated clearance of neutrophils

Bo Ri Seo[1,2], Christopher J. Payne[1,2,3†], Stephanie L. McNamara[1,2†], Benjamin R. Freedman[1,2], Brian J. Kwee[1,2], Sungmin Nam[1,2], Irene de Lázaro[1,2], Max Darnell[1,2], Jonathan T. Alvarez[1,2], Maxence O. Dellacherie[1,2], Herman H. Vandenburgh[4], Conor J. Walsh[1,2], David J. Mooney[1,2*]

Mechanical stimulation (mechanotherapy) can promote skeletal muscle repair, but a lack of reproducible protocols and mechanistic understanding of the relation between mechanical cues and tissue regeneration limit progress in this field. To address these gaps, we developed a robotic device equipped with real-time force control and compatible with ultrasound imaging for tissue strain analysis. We investigated the hypothesis that specific mechanical loading improves tissue repair by modulating inflammatory responses that regulate skeletal muscle regeneration. We report that cyclic compressive loading within a specific range of forces substantially improves functional recovery of severely injured muscle in mice. This improvement is attributable in part to rapid clearance of neutrophil populations and neutrophil-mediated factors, which otherwise may impede myogenesis. Insights from this work will help advance therapeutic strategies for tissue regeneration broadly.

INTRODUCTION

Skeletal muscle injury caused by traumatic accidents, tumor resections, and ischemia-reperfusion impairs posture and functional locomotion, which ultimately limits activities of daily living and diminishes quality of life (*1*, *2*). Extensive defects (20% or more muscle mass loss) require therapeutic interventions to support functional regeneration (*1*, *2*). Regenerative muscle fiber formation and maturation are critical for functional repair, and this is led by the activity of transcription factor paired box 7 (Pax7)–expressing muscle progenitor cells (MPCs) or satellite cells (*3*). The regenerative process coincides with a sequence of immune cell infiltration and activation. Immune cells partake in the clearance of damaged muscle fibers; the specific cytokines and growth factors secreted by these cells modulate the sequence of satellite cell activation and differentiation and instruct neighboring stromal cells to participate in extracellular matrix (ECM) remodeling and angiogenesis (*3*). As such, immunomodulation to facilitate skeletal muscle regeneration is an emerging therapeutic strategy (*1*, *3*). Delivery of immunomodulatory agents to an injury site has shown promise in preclinical studies (*4*–*6*). Certain materials available for filling muscle defects in the clinic (*7*) have been proposed to stimulate a prohealing immune axis (*8*). However, surgical intervention with autologous muscle flaps is still the standard strategy for patients with severe muscle injury, despite morbidity at the donor sites (*1*). A simple, noninvasive therapy for the treatment of severe skeletal muscle injury remains an unmet clinical need.

Mechanotherapy, application of mechanical loading (ML) to injured tissue (e.g., massage therapy), has been widely used as an alternative and complementary medicine (*9*) and is known to improve rehabilitation of musculoskeletal tissues, possibly by increasing blood flow, reducing inflammation, and increasing mitochondrial biogenesis (*10*, *11*). However, highly variable methods (e.g., external volume expansion, passive stretching, and varied compression devices) and parameters of ML used by different researchers limit comparisons and meaningful conclusions regarding the efficacy of mechanotherapy (*12*–*15*). In addition, mechanotherapy has primarily been tested in the setting of exercise-mimicking skeletal muscle injuries (e.g., eccentric exercise) (*11*, *16*), but its effects on severe muscle injury are unclear. Clinical and preclinical studies suggest that mechanotherapy may attenuate inflammatory responses to accelerate repair of muscle injury; however, a direct connection between specific cellular and molecular components of reduced inflammation and functional regeneration has not been clearly identified.

RESULTS

Robotic actuator delivers programmable and quantifiable controlled compressive forces to murine skeletal muscle

This study aimed to identify therapeutic regimens of noninvasive mechanotherapy applied to severe skeletal muscle injury and to probe the functional link between ML and regeneration. First, we developed external robotic devices to apply controlled and quantifiable compressive forces to the tibialis anterior (TA) muscle in rodents (Fig. 1). Several studies have previously developed robotic systems that deliver ML in a controlled manner in the form of implants (*17*, *18*) or external loading devices (*12*, *14*). In the present approach, an external robotic device was designed to deliver compressive loading to the TA muscle through a soft interface as a noninvasive therapeutic tool (movie S1). The robotic device uses an electromagnetic actuator (i) and force sensor assembly covered with soft silicone (ii), which allows continuous measurement of the applied compressive load. A customizable silicone-based mount (iii and iv) was designed to position and restrain the mouse limb during loading, and this allowed consistent support of the limb position (Fig. 1A). The robotic assembly is easily replicated for concurrent stimulation of multiple mice (fig. S1). Moreover, the device uses a force-feedback loop scheme (Fig. 1B), which allows precise application of preprogrammed force profiles to muscle tissues (Fig. 1C). These force profiles can be programmed to generate mechanical loads of arbitrary

[1]John A. Paulson School of Engineering and Applied Sciences, Harvard University, Cambridge, MA 02138, USA. [2]Wyss Institute for Biologically Inspired Engineering, Harvard University, Boston, MA 02115, USA. [3]Viam Inc., New York, NY 10023, USA. [4]Department of Pathology and Lab Medicine, Brown University, Providence, RI 02912, USA.
*Corresponding author. Email: mooneyd@seas.harvard.edu
†These authors contributed equally to this work.

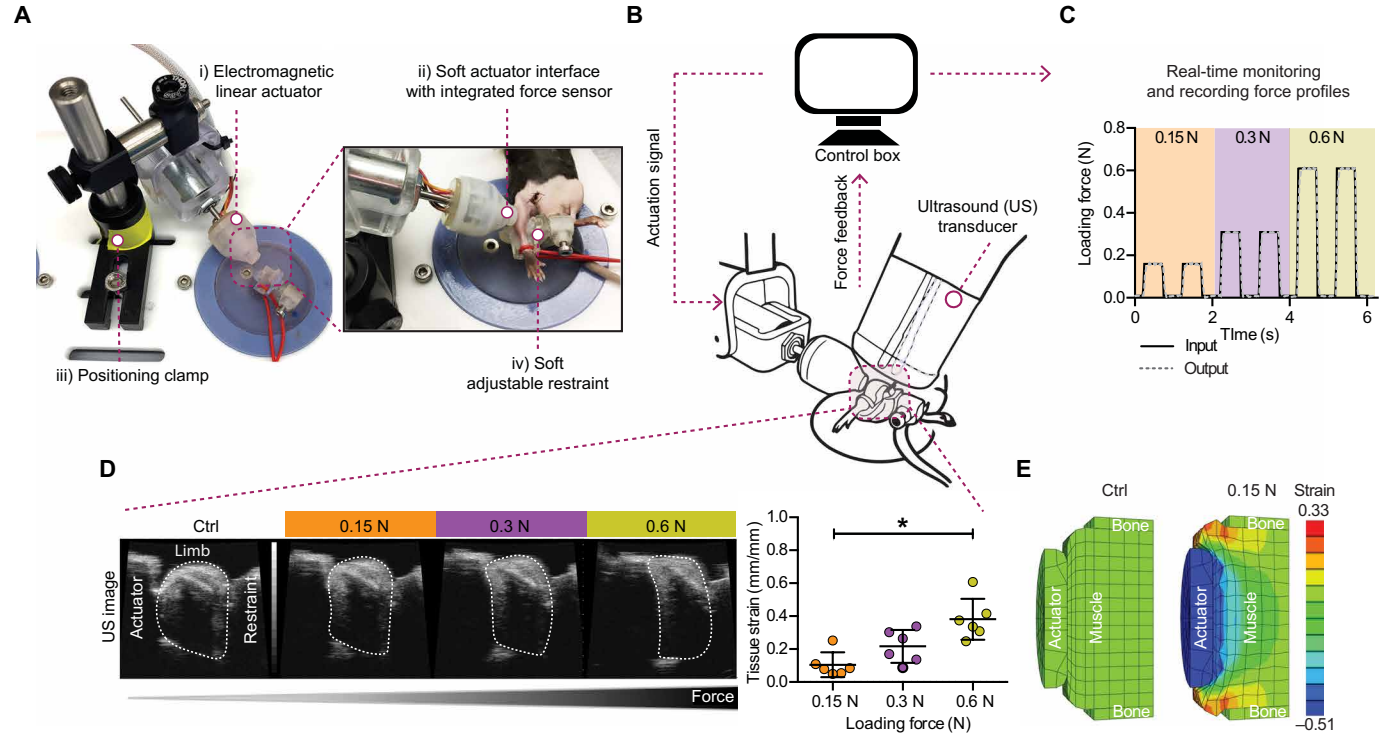

Fig. 1. Electromagnetic linear actuator with integrated force sensor delivers reproducible compressive loading to muscle tissue. (**A**) Photograph of robotic soft-interface actuator equipped with a force sensor and demonstration of the actuator positioned toward the injured tibialis anterior (TA) muscle of hindlimb of mouse. (**B**) Schematic illustration of the design and force-control mechanism of the actuator and setup with ultrasound transducer for real-time tissue monitoring. (**C**) Real-time monitoring of input and output loading force profiles (0.15, 0.3, and 0.6 N). (**D**) Representative ultrasound images of TA muscle captured during ML with 0.15, 0.3, and 0.6 N compressive forces and a scatter dot plot of corresponding tissue strains. (**E**) Representative strain heatmap of TA muscle obtained from computational simulation without or with ML (Ctrl versus 0.15 N). ($n = 6$ per condition, means ± SD). *$P < 0.05$, determined by Kruskal-Wallis test with post hoc Dunn's tests.

magnitude, frequency, duty cycle, and shape (e.g., step, trapezoidal sawtooth, or sinusoidal). An additional mounting system is used to position a high-frequency ultrasound (US) transducer over the loaded TA muscle to visualize overall tissue deformation in the stimulated limb (movie S2). This allows quantification of tissue strain in the stimulated region as a function of loading force magnitude (Fig. 1D). We also developed a computational model of tissue strain distributions under specific forces and validated the model predictions of tissue strain under specific loading with experimental data obtained from US image analysis (Fig. 1E and table S1). This computational model allows prediction of tissue strains as the tissue properties and loading parameters are altered.

Muscle cells respond to the magnitude of loading in vitro (*19*); therefore, we explored the effect of loading force in a mouse model of severe TA muscle injury (*20*). Initial studies revealed that forces below 0.15 N did not reduce fibrosis when compared with an untreated group (fig. S2). Forces larger than 0.6 N led to visual physical damage to the skin, which prevented their use in these studies. All subsequent studies focused on a force range of 0.15 to 0.6 N, which corresponded to muscle strains of 10 to 40% (Fig. 1D and table S1). The Young's moduli of injured TA muscle did not significantly change over time in the absence and presence of ML (fig. S3), indicating that the strain that each TA muscle experienced under the specific magnitude of force was comparable over time. Other loading parameters were adapted from a previous study (*20*) and were kept constant [1 Hz, square wave, 20% (on)/80% (off) duty cycle, 5 min of loading every 10 to 12 hours].

Robotic compressive loading improves functional recovery of severely injured skeletal muscle

Three different forces (0.15, 0.3, or 0.6 N) were applied using ML starting 1 day after injury and continued daily up to 14 days, whereas mice in the control group remained untreated (Fig. 2A). Application of the three different forces was subsequently found to lead to a significant reduction ($P < 0.05$) in interstitial fibrosis and damaged muscle fibers in the TA (Fig. 2, B to D), with no significant difference between the three different force conditions. The cross-sectional area (CSA) of the muscle fibers, which is indicative of muscle growth and contractile strength (*21*), showed consistently larger myofibers in the ML-treated muscle (Fig. 2E). Last, to assess whether the ML-mediated improvements in histological features of injured muscle correlated with muscle strength recovery, the tetanic force of TA muscles was measured. TA muscle weight was not significantly different across the conditions (Fig. 2F), but TA muscles treated with ML at all three force conditions exhibited higher tetanic forces than the untreated control group, with no significant differences between the three ML groups (Fig. 2, G and H). In addition, TA muscle treated with ML exhibited even greater contractile force than uninjured TA muscle. Because all ML groups led to equivalent improvements in muscle repair, only the 0.3N group was selected for subsequent studies. The kinetics of injured muscle recovery with and without ML revealed a continuously increasing tetanic force with ML (fig. S4), suggesting that ML accelerates the rate of tissue regeneration. Quantitative reverse transcription polymerase chain reaction (RT-qPCR) analysis indicated that the expression of embryonic (*Myh3*) and

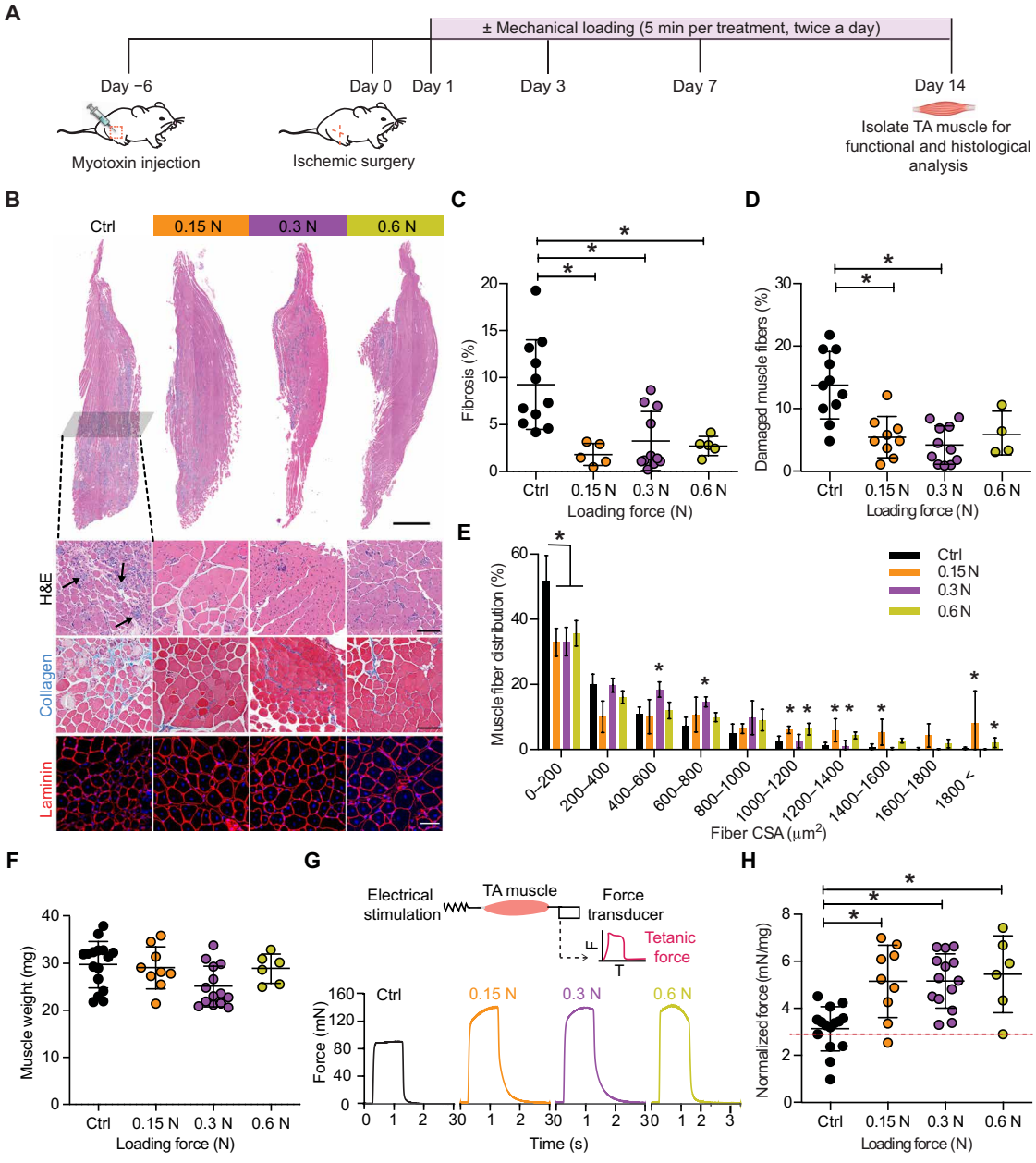

Fig. 2. Cyclic loading improves skeletal muscle regeneration after severe injury. (**A**) Experimental design and time line of TA muscle injury, ML treatment, and analysis in mice. (**B**) Representative hematoxylin and eosin (H&E) images of longitudinal histological sections of TA and its cross sections stained with H&E (top), Masson's trichrome (collagen in blue, center), and laminin (bottom). Scale bars, 1 mm (entire TA) and 100 μm (cross sections). (**C** to **G**) Quantification of (C) fibrotic regions (appearing as blue in Masson's trichome in B), (D) damaged muscle fibers (indicated by black arrows in H&E in B), (E) cross-sectional areas of muscle fibers, (F) muscle weight measured at the end point, (G) representative tetanic force graphs, and (**H**) measurement of normalized contraction force of TA muscle after 14-day treatment for control (no loading) and ML with various forces after the injury. Red dashed line indicates the contraction forces from uninjured TA muscle. Data in (C) to (G) are means ± SD ($n = 4$ to 16 per condition), and $^*P < 0.05$, determined by Kruskal-Wallis test with post hoc Dunn's tests.

perinatal (*Myh8*) myosin heavy chains (MyHCs), usually activated upon injury, were down-regulated by day 7, whereas expression of adult MyHCs (*Myh4* and *Myh7*) was up-regulated with time or/and ML treatment (fig. S5). In contrast, vascular perfusion measured by laser Doppler imaging slowly recovered in the injured limbs, with no notable impact of ML (fig. S6). These findings indicate that a specific range of forces and the corresponding strains promote functional recovery of severely impaired muscle.

Compressive loading rapidly reduces proinflammatory factors linked with neutrophil trafficking

To explore whether ML alters local immune responses in treated tissues, the quantity of a broad range of inflammatory factors (cytokines and chemokines) from TA muscle undergoing ML was quantified over time. The relative ratio of each factor in the ML-treated group to control group was compared over time (Table 1). Most factors demonstrated a decrease, of varying degree, with ML on day 3.

Table 1. List of cytokines and chemokines analyzed and the relative ratio of their expression in TA muscle from ML-treated compared with untreated mice at three different time points. D, day; Ctrl, control (untreated).

Ratio of ML over Ctrl

Cytokine name	D3	D7	D14
Adiponectin/Acrp30	1.005	0.741	1.402
Amphiregulin	0.280	0.687	0.813
Angiopoietin-1	0.277	0.692	0.844
Angiopoietin-2	0.529	0.814	0.652
Angiopoietin-like 3	0.641	0.947	0.804
Baff/BLyS/Tnfsf13b	0.410	0.729	1.132
C1q R1/CD93	1.087	0.874	1.163
Ccl2/JE/Mcp-1	0.323	0.677	0.630
Ccl3/Ccl4 Mip-1 alpha/beta	0.327	0.849	0.565
Ccl5/Rantes	0.342	0.642	0.826
Ccl6/C10	1.066	0.829	1.633
Ccl11/Eotaxin	0.659	0.766	1.337
Ccl12/Mcp-5	0.615	0.613	0.992
Ccl17/Tarc	0.506	0.907	0.979
Ccl19/Mip-3 beta	0.124	0.748	0.888
Ccl20/Mip-3 alpha	0.404	1.324	0.966
Ccl21/6Ckine	0.931	0.960	1.268
Ccl22/Mdc	0.263	0.703	0.712
CD14	0.490	0.820	1.296
CD40/Tnfrsf5	0.852	0.781	1.068
CD160	0.989	0.957	1.440
Chemerin	0.573	0.938	1.050
Chitinase 3-like 1	0.847	0.426	0.836
Coagulation factor III/tissue factor	1.048	0.898	1.233
Complement component C5/C5a	0.390	0.774	0.921
Complement factor D	0.972	0.848	2.046
C-reactive protein/Crp	0.997	0.712	1.663
Cx3cl1/Fractalkine	0.086	0.759	0.562
Cxcl1/Kc	0.378	0.689	0.452
Cxcl2/Mip-2	0.005	0.738	0.741
Cxcl9/Mig	0.337	0.770	1.004
Cxcl10/IP-10	0.316	0.796	1.361
Cxcl11/I-Tac	0.011	0.866	1.095
Cxcl13/Blc/Bca-1	0.353	0.866	0.952
Cxcl16	0.668	0.997	0.791
Cystatin C	0.868	1.035	1.159
Dkk-1	0.011	0.891	0.758
Dppiv/CD26	0.858	0.952	1.147
Egf	0.522	1.028	0.563
Endoglin/CD105	0.957	0.863	1.162

continued on next page

Ratio of ML over Ctrl			
Endostatin	0.966	0.895	1.280
Fetuin A/Ahsg	0.923	0.915	1.423
Fgf acidic	1.263	1.098	1.047
Fgf-21	0.550	1.124	1.295
Flt-3 ligand	0.709	0.905	1.527
Gas 6	0.678	0.954	0.994
G-csf	0.010	1.011	1.138
Gdf-15	0.009	1.014	0.812
Gm-csf	0.020	0.982	0.759
Hgf	0.717	0.825	0.805
Icam-1/CD54	1.023	0.871	1.012
Ifn-gamma	0.011	0.960	0.892
Igfbp-1	0.691	0.703	0.985
Igfbp-2	0.836	0.721	1.187
Igfbp-3	0.809	1.104	0.937
Igfbp-5	1.187	1.217	1.251
Igfbp-6	0.989	1.104	1.215
Il-1 alpha/Il-1F1	0.426	0.898	0.926
Il-1 beta/Il-1F2	0.017	1.148	0.911
Il-1ra/Il-1F3	0.768	1.016	0.390
Il-2	1.000	0.768	0.622
Il-3	0.195	0.788	0.826
Il-4	1.128	0.888	1.261
Il-5	0.229	0.977	1.048
Il-6	0.019	0.555	1.021
Il-7	0.588	0.899	1.357
Il-10	0.017	1.017	1.175
Il-11	0.347	1.026	1.035
Il-12p40	0.219	0.733	1.156
Il-13	0.025	0.792	1.194
Il-15	0.028	0.946	1.197
Il-17a	0.043	0.499	0.386
Il-22	1.000	0.873	0.938
Il-23	0.111	0.836	0.956
Il-27p28	0.949	1.092	1.471
Il-28	1.011	0.906	1.391
Il-33	1.032	0.797	1.034
Ldl R	0.844	0.946	1.090
Leptin	0.051	0.846	1.571
Lif	0.506	1.003	1.592
Lipocalin-2/Ngal	0.847	0.496	1.099
Lix	0.490	0.902	1.717
M-csf	0.724	1.010	1.306
Mmp-2	1.039	1.057	1.184

continued on next page

Ratio of ML over Ctrl			
Mmp-3	0.636	1.034	1.080
Mmp-9	0.431	0.599	0.398
Myeloperoxidase	0.900	0.381	1.345
Osteopontin	1.058	0.781	1.772
Osteoprotegerin/Tnfrsf11b	0.611	0.669	1.372
Pd-ecgf/thymidine phosphorylase	0.349	0.764	1.650
Pdgf-bb	0.960	1.387	1.747
Pentraxin 2/Sap	0.493	0.830	1.446
Pentraxin 3/Tsg-14	0.892	0.634	0.863
Periostin/Osf-2	1.086	1.017	1.012
Pref-1/Dlk-1/Fa1	1.004	1.244	0.991
Proliferin	0.686	1.029	1.446
Proprotein convertase 9/Pcsk9	0.608	0.799	1.574
Rage	0.469	0.785	1.218
Rbp4	0.939	0.842	1.483
Reg3G	0.841	0.719	2.537
Resistin	1.162	0.944	1.345
E-selectin/CD62E	0.235	0.668	1.487
P-selectin/CD62P	0.985	0.992	1.136
Serpin E1/Pai-1	1.024	0.791	0.974
Serpin F1/Pedf	0.907	1.174	0.990
Thrombopoietin	0.448	1.146	1.170
Tim-1/Kim-1/Havcr	0.365	0.955	1.214
Tnf-alpha	0.352	0.870	1.304
Vcam-1/CD106	0.968	0.899	1.268
Vegf	0.929	0.939	2.034
Wisp-1/Ccn4	1.071	0.836	0.858

The quantity of most factors in both ML and control limbs were similar at days 7 and 14. The cytokines most diminished by ML (>50% reduction relative to the untreated control group) at day 3 were visualized using a heatmap (Fig. 3A). Gene enrichment analysis revealed that those significantly reduced cytokines were associated with inflammatory responses and granulocyte or myeloid leukocyte migration, specifically neutrophil chemotaxis and migration (Fig. 3A and table S2). We next assessed whether the altered cytokine profiles were linked with any changes in specific subsets of immune cell populations within the injured muscle. The numbers of total $CD45^+$ immune cells, $CD11c^-/CD11b^+/F4/80^+/Ly6g^-$ monocytes/macrophages, $CD11c^+/CD11b^+$ dendritic cells, and $CD4^+$ T cells increased and reached a peak on day 3 or 7, and then decreased to low numbers at day 14 both in the untreated control and ML-treated tissue; no significant differences between the two conditions were noted for these cell types at all time points (fig. S7). In addition, the subtypes of macrophages were screened because specific subtypes of macrophages are considered to play key roles in tissue regeneration (*3*). Similar numbers of $F4/80^+/CD86^+/CD80^+$ proinflammatory or M1 macrophages and $CD206^+$ prohealing or M2 macrophages were found in ML as compared with control mice at both time points analyzed (fig. S8). Depletion of macrophages had no impact on the positive influence of ML on muscle regeneration (fig. S9). The numbers of $Ly6g^+/Ly6c^{intermediate}$ neutrophils in both groups were initially high and decreased over time. However, in comparison with control muscles, ML-treated muscles exhibited a significant reduction ($P < 0.05$) in neutrophils at 3 days (Fig. 3B). Spatially, neutrophils and their peroxidase enzyme, myeloperoxidase (Mpo), were apparent in broad regions of the control muscles, whereas they were present only in limited areas of ML-treated muscles (Fig. 3C and fig. S10). Statistically insignificant but decreasing trends in the neutrophil population on day 3 were also found in animals treated with 0.15 and 0.6 N (fig. S11) that promoted similar recovery of the injured muscle (Fig. 2). This finding is aligned with the results of the cytokine array analysis, suggesting that decreased quantity of cytokines stimulating neutrophil chemotaxis and migration is responsible for the rapid decrease in neutrophils within the ML-treated muscle. One possible mechanism for this observed reduction in intramuscular cytokines

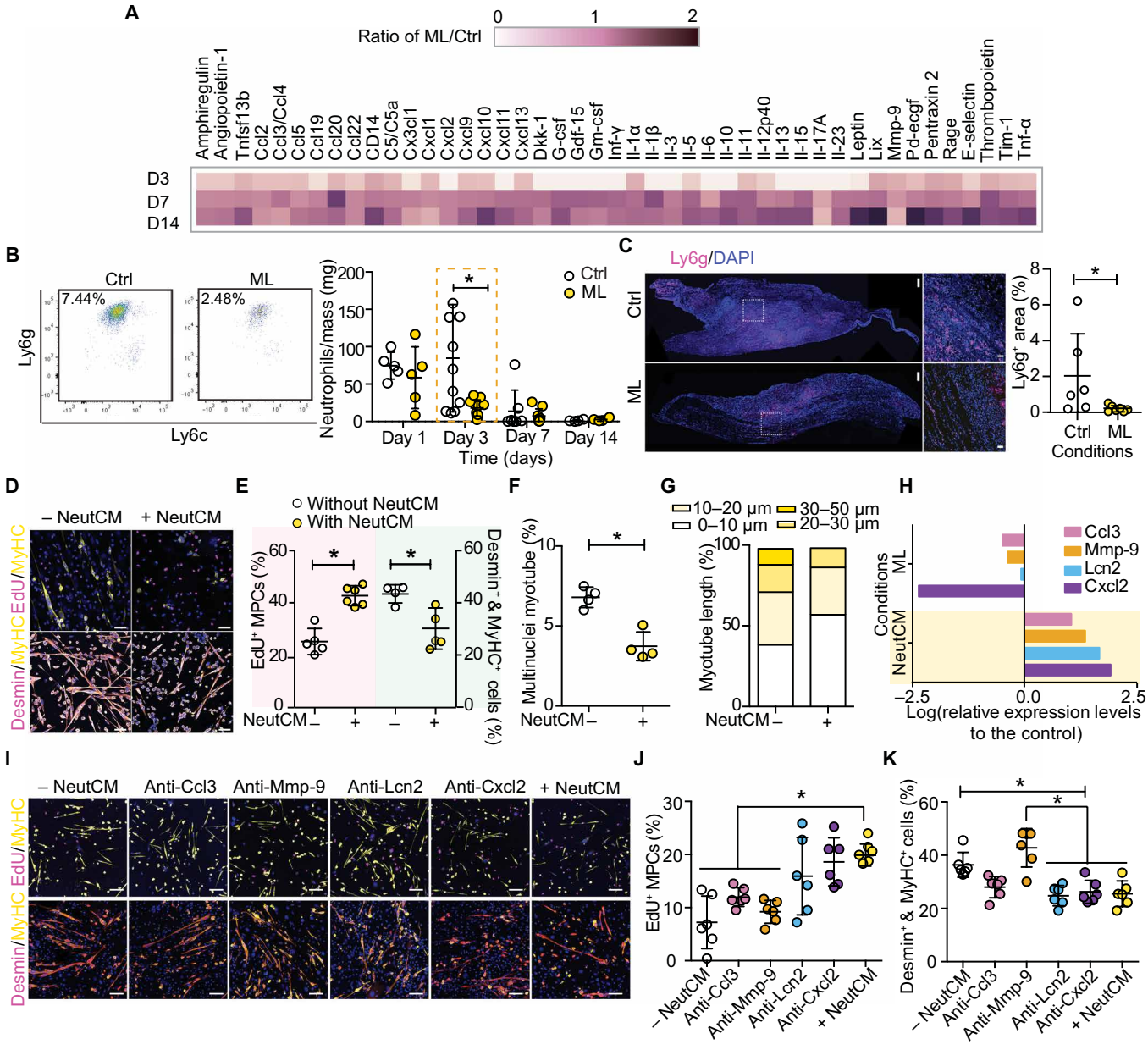

Fig. 3. ML mediates rapid clearance of cytokines and neutrophils with effects on MPCs. (**A**) Heatmap of a subset of cytokines in injured TA muscle with and without mechanical stimulation for 3 to 14 days (D3, D7, and D14). Data are represented as values in tissues treated with ML normalized to the untreated control tissue at the same time point. (**B** and **C**) Representative flow, dot plot, and immunofluorescence images on day 3 and quantification of neutrophil populations in muscle tissue without and with ML (0.3 N) for 14 days. Both pressure cuff and robotic actuator were used for mechanical stimulation. Scale bars, 500 and 50 μm, respectively ($n = 4$ to 12 per condition, means ± SD). *$P < 0.05$ determined by two-way ANOVA with Bonferroni's multiple comparison tests and unpaired two-tailed Mann-Whitney test, respectively. (**D**) Immunofluorescence micrographs visualizing proliferation of MPCs (top) stained for EdU, MyHC, and DAPI and differentiation of MPCs (bottom) with desmin, MyHC, and DAPI staining after 3- or 5-day treatment with neutrophil-conditioned medium (+NeutCM) or control medium (–NeutCM), respectively. Scale bars, 100 μm. (**E** to **G**) Quantification of (E) EdU$^+$ or MyHC$^+$/desmin$^+$ cell populations, (F) the population of multinucleated myotubes, and (G) distribution of myotube lengths, respectively. ($n = 4$ to 6 per condition, means ± SD). $P < 0.05$ (*) determined by unpaired two-tailed Mann-Whitney test. (**H**) Bar graphs of relative expression in log scale in NeutCM (relative to basal media) and TA muscle (ML-treated group versus control group). (**I**) Immunofluorescence micrographs visualizing proliferation of MPCs stained for EdU, MyHC, and DAPI and differentiation of MPCs with desmin, MyHC, and DAPI staining after 3- or 5-day treatment without and with NeutCM primed with neutralizing antibodies to different factors, and (**J**) quantification of EdU$^+$ MPC populations and (**K**) desmin$^+$/MyHC$^+$ double positive myoblast populations ($n = 6$ per condition, means ± SD). Scale bars = 100 μm. *$P < 0.05$ determined by Kruskal-Wallis test with post hoc Dunn's tests.

may be an ML-driven flushing of tissue cytokines out of the injured tissue: Greater dispersion of intramuscularly injected fluorescent dextrans of various molecular weights (10 to 155 kDa) was observed throughout the mechanically loaded tissue as compared with control (fig. S12). The alteration in neutrophils in the ML-treated tissues was not reflected in systemic effects because neutrophil populations in

other organs, including lung, bone marrow, and spleen, were comparable between the two conditions (fig. S13). These findings demonstrate that ML mediates local immunomodulatory effects in severely injured TA muscle, specifically through neutrophil-mediated effects in the early phases of the immune response.

Neutrophil-mediated factors regulate proliferation and differentiation of MPCs

Although the role of neutrophils in clearing damaged cells and invading microorganisms has been well described (*22*), their impact on MPC behaviors during muscle regeneration is unclear. Thus, the effects of neutrophil-secreted factors on myogenesis were assessed by culturing freshly isolated MPCs with conditioned media collected from activated neutrophil cultures. These in vitro studies indicated that neutrophil-conditioned media (NeutCM) significantly increased the number of proliferating MPCs relative to those cultured with control media (Fig. 3, D and E). However, the differentiation of MPCs was significantly reduced when cultured with NeutCM, as indicated by the decreased number of desmin$^+$ and MyHC double-positive multinucleated myotubes and their immature morphological features (Fig. 3, D to G). These data suggest that neutrophil-secreted factors stimulate proliferation of MPCs, yet the prolonged presence of those factors impairs myogenesis. NeutCM was also screened using the same cytokine panel used to characterize TA muscle after ML (fig. S14), and the results from the two analyses were compared. Cxcl2/Mip2, Lipocalin-2/Ngal (Lcn2), Mmp-9, and Ccl3/Ccl4 were found to be prominent in NeutCM while being significantly diminished in muscles subjected to ML (Fig. 3H). The secretory phenotypes of neutrophils isolated from ML-treated and untreated TA muscle were not distinct (fig. S15), indicating that the reduction of such cytokines with ML resulted from the decreased number of intramuscular neutrophils. MPC proliferation and differentiation were analyzed in vitro in the presence of neutralizing antibodies for each of these agents in NeutCM. The proliferation of MPCs cultured with NeutCM containing neutralizing antibodies against Ccl3 and Mmp-9 was significantly decreased and was similar to the control group (no NeutCM exposure; Fig. 3, I and J). Neutralization of Lcn2 or Cxcl2 in NeutCM had moderate or no impact on proliferation (Fig. 3, I and J). On the other hand, the populations of desmin$^+$/MyHC$^+$ myoblasts, elongated myofibers, and multinuclei myotubes were significantly increased when inhibiting Mmp-9 from NeutCM, whereas neutralizing the other agents in NeutCM did not recover the decreased MPC differentiation with NeutCM (Fig. 3, I and K, and fig. S16). These in vitro studies reveal that neutrophil-derived, secreted factors promote proliferation but impede myogenic commitment of MPCs, and Ccl3 and Mmp-9 play important roles in these effects.

ML facilitates myogenesis and recovery of mature muscle fiber type composition

Next, the effect of ML on early myogenic features was evaluated. Similar to in vitro results, significantly increased populations of cells expressing MyoD, a myogenic regulator, and elongated desmin$^+$ myotubes were found in ML-treated tissue, as compared with the untreated group (Fig. 4, A and B, and fig. S17). No significant increase in the Pax7$^+$ cell population was observed (Fig. 4C). Because extrinsic mechanical cues can also affect myogenic activities through mechanotransduction pathways such as myocardin-related transcription factor A (MRTF-A) (*23*, *24*), its expression was analyzed. Immunofluorescence image analysis and Western blot analysis revealed that more than 50% of the total cell population expressed Mrtf-a in both untreated and ML-treated muscle on days 3 and 14 after injury, whereas uninjured TA muscle had a smaller proportion (~15% of total cell population) positive for Mrtf-a (fig. S18, A to D). The majority of MyoD$^+$ cells coexpressed Mrtf-a in both conditions, whereas the total number of MyoD$^+$ cells was still significantly greater ($P < 0.05$) in ML-treated TA muscle (fig. S18, E and F). These findings suggest that injury primarily activates Mrtf-a signaling and that the Mrtf-a–activated MyoD$^+$ cell population increased with ML.

Next, we examined whether ML treatment at an acute phase of injury is sufficient to achieve full functional recovery. Injured muscle treated with ML for the first 7 days, but no ML for the following 7 days, generated contractile forces between the control group without ML and the group treated with ML for the full 14 days (fig. S19). These data suggest that ML at an early stage is necessary but not sufficient for full functional recovery. We then sought to understand whether ML further helps restore a normal composition of muscle fiber types over time in regenerating muscle. Each muscle tissue contains distinct compositions of muscle fiber types depending on its anatomy and functionality. The composition of fiber types can change because of physical training or disuse, injury, and aging, and this potentially affects the strength and functional performances of muscle tissue (*25*, *26*). Muscle fiber phenotyping was performed on injured TA muscle treated with and without ML for 14 days and compared to healthy TA muscle (Fig. 4, D and E, and fig. S20). In healthy TA muscle, type IIB fibers were the most abundant fiber type, constituting 50% or more of total muscle fibers, and this trend remained similar for the injured TA muscle in both conditions (Fig. 4, E and F). Type IIX fibers were similarly high in healthy TA muscle and ML-treated injured TA muscle (Fig. 4G). In contrast, untreated TA muscle contained smaller numbers of type IIX fibers and increased numbers of type IIA, relative to ML-treated and healthy TA muscle (Fig. 4, G and H). Murine TA muscle contains a small number of type I fibers. A small increase in type I fiber was noted in ML-treated and healthy TA muscle as compared with untreated injured TA muscle, but there was no significant difference across the conditions (Fig. 4I). The higher content of type IIX fibers and smaller portion of IIA fibers are consistent with the enlarged fiber size and greater force production of ML-treated muscle (Fig. 2) (*27*, *28*).

The expression and activity of peroxisome proliferator–activated receptor-gamma coactivator (PGC) 1α and β, transcriptional factors that drive muscle fiber type conversion (*29*), are known to suppress proinflammatory signaling pathways, such as the nuclear factor κB (NF-κB) pathway and vice versa (*30*, *31*). The expression of *Pgc-1α* showed an increasing trend with ML and time, whereas the expression of the *Nf-κb* pathway concomitantly decreased (fig. S21, A and B). The expression of *Pgc-1*β was not significantly different between control and ML-treated groups (fig. S21C), but it is possible that the activity of *Pgc-1*β may be modified at a posttranslational stage (*32*), which was not explored in this study. These data suggest that ML can promote restoration of mature muscle fiber type during regeneration.

Temporal depletion of neutrophils after injury improves skeletal muscle repair

Last, to directly probe the role of neutrophils in muscle regeneration, neutrophils were depleted in injured mice during the first 3 days after ischemia injury (Fig. 5A), mimicking the clearance of neutrophils over this time frame that was observed with ML (Fig. 3B).

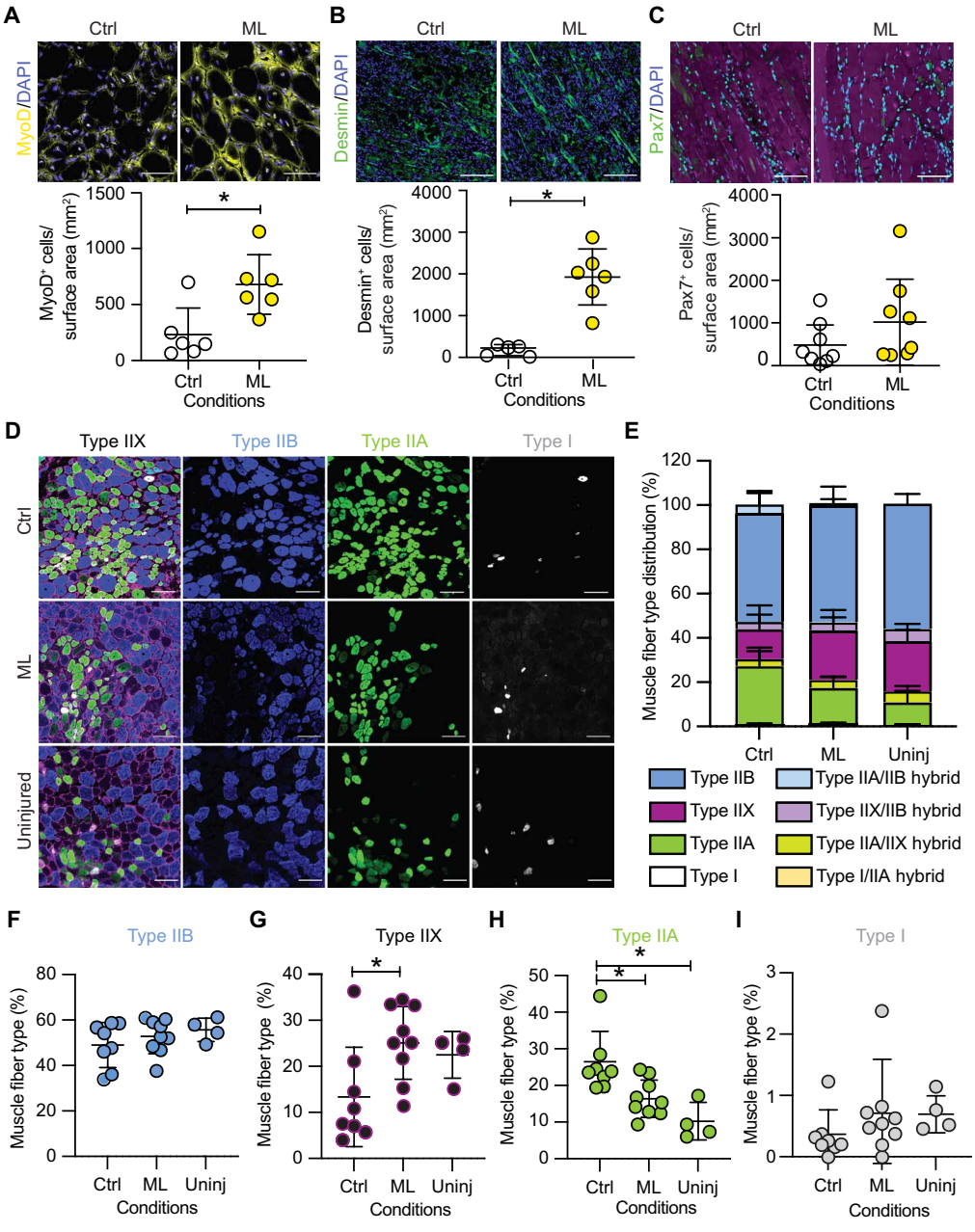

Fig. 4. ML accelerates myogenesis and recovery of mature muscle fiber type composition. (**A** to **C**) Representative immunofluorescence images and quantification of (A) MyoD$^+$, (B) desmin$^+$, and (C) Pax7$^+$ MPCs in injured murine TA muscle after 3-day treatment with ML. Scale bars, 50 μm ($n = 6$ to 8 per condition, means ± SD), and $^*P < 0.05$, determined by unpaired two-tailed Mann-Whitney test. (**D** and **E**) Immunofluorescence images and stacked bar graphs visualizing muscle fiber type compositions of injured TA muscle treated without and with ML for 14 days relative to uninjured TA muscle. Scale bars, 50 μm. (**F** to **I**) Quantification of muscle fiber subtypes of TA muscle: (F) type IIB (blue), (G) type IIX (black), (H) type IIA (green), and (I) type I (white). Magenta is laminin ($n = 4$ to 9 per condition, means ± SD), and $^*P < 0.05$ determined by Kruskal-Wallis test with post hoc Dunn's tests.

Mice treated with an anti-Ly6g antibody exhibited significantly reduced muscle damage and fibrosis as compared with the group treated with a respective control antibody (Fig. 5, B to D). Analysis of muscle fiber size revealed that both ML and neutrophil depletion led to a similar distribution skewed toward larger fibers (Fig. 5E). Injured muscles subjected to neutrophil depletion exhibited greater recovery of contractile forces compared with untreated muscles, and the effect of neutrophil depletion with anti-Ly6g antibody on functional recovery was similar to the effect of ML (Fig. 5F). These findings indicate that temporal control of neutrophil abundance in damaged muscle is associated with the effects of ML on muscle regeneration in this injury model.

DISCUSSION

Here, we used a robotic system capable of applying varied ML in a controlled manner to identify a therapeutic range of forces and corresponding tissue strains for muscle regeneration in mice. A therapeutic regimen of tissue strain for severely injured muscle tissue has not been previously reported. Some in vitro studies have shown that responses to ML at the cellular level are dependent on the amplitude of strain (*19*, *33*), and future studies to assess how tissue strain translates to cellular strain may further help define the therapeutic regimen of ML and cellular mechanisms underlying its effects. Our studies also link ML-mediated muscle regeneration with specific immunomodulatory features, establishing an intersection of the currently distinct fields of mechanotherapy and immunotherapy.

The ability of this robotic system to enable compressive loading and tissue strain to be applied reproducibly and systematically contrasts with the lack of control in manual mechanical manipulation of muscle tissues (*9*). The scalability of robotic systems increases the feasibility of large-scale studies, and unlike traditional rigid robotic devices, the soft-interface actuator and limb holder in the current device help minimize safety concerns and potential inconsistencies. Demonstration of the technology in large-scale studies is beyond the scope of this work, but designing and building actuators for human muscle application will help demonstrate the scalability of our strategy in future studies (*34*, *35*). Using computational modeling to predict

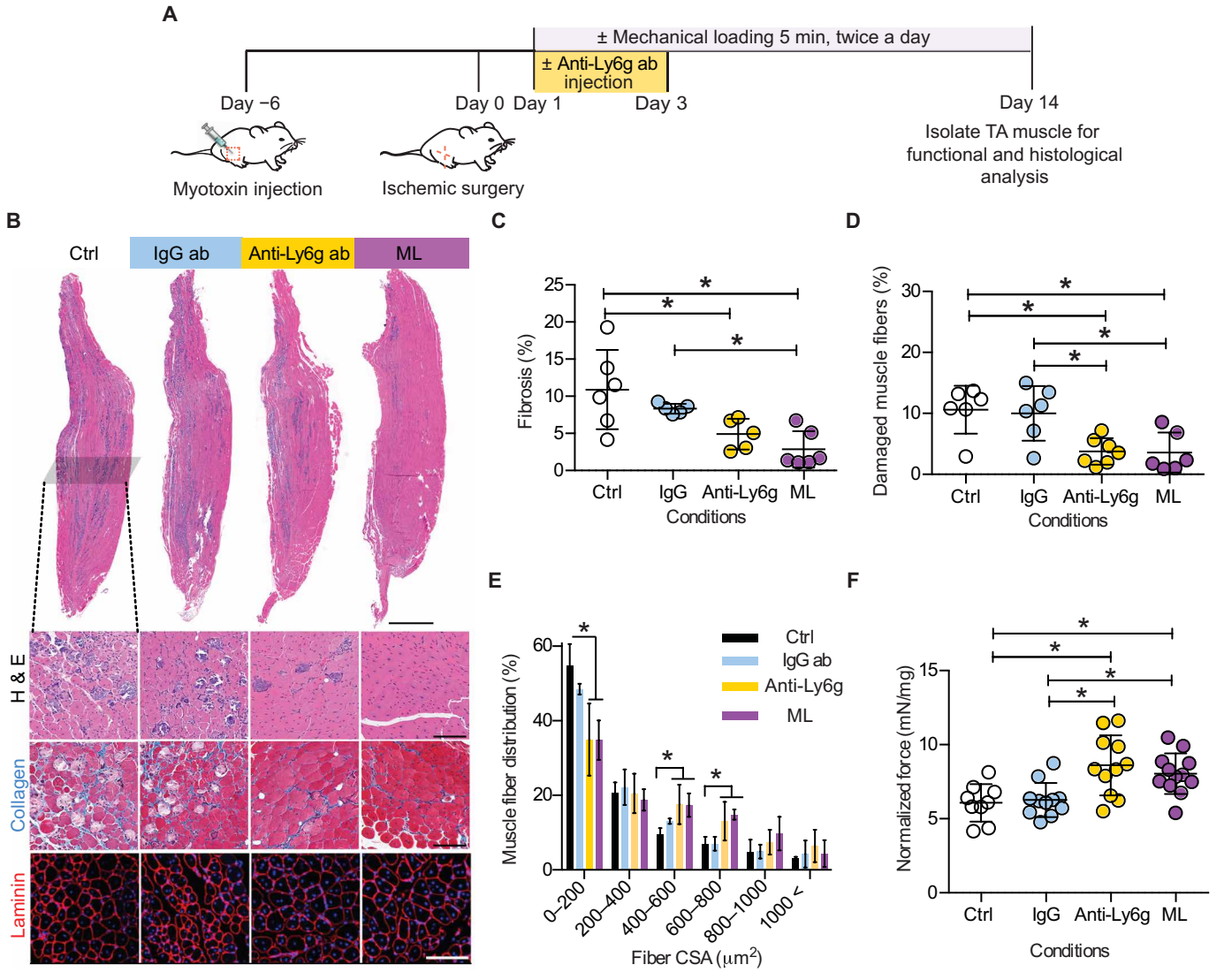

Fig. 5. Antibody-mediated clearance of neutrophils mimics the effects of ML on muscle regeneration. (**A**) Experimental design and time line of temporal depletion of neutrophils using treatment with anti-Ly6g antibody or ML on injured TA muscle in mice. (**B**) Representative H&E images of longitudinal and cross sections of TA muscle (top) treated without and with anti-Ly6g antibody or ML and associated tissue cross section stained with Masson's trichrome (center) and stained for laminin (bottom). Scale bars, 1 mm and 100 μm, respectively. (**C** to **F**) Quantification of (C) fibrotic regions (interstitial blue regions in Masson's trichrome in B), (D) damaged muscle fibers (H&E in B), and (E) measurement of CSAs of muscle fibers based on laminin-stained samples and (F) normalized contraction force of TA muscle 14 days after injury ($n = 6$ to 16 per condition, means ± SD), and *$P < 0.05$, determined by one-way ANOVA with post hoc Tukey's tests.

tissue strain can also provide quantitative guidelines for loading conditions in future large animal–based preclinical trials and potentially in future clinical trials.

As a potential link between ML and regenerative immune responses, we found that ML led to early clearance of neutrophils from damaged muscle. A previous report also showed that cyclic compressive loading applied immediately after eccentric exercise–induced injury led to a reduction in the number of inflammatory neutrophils and macrophages within muscle (*16*), but this trend is possibly context dependent because load-dependent increases in macrophage populations were previously found in healthy rat TA muscle subjected to massage (*12*). ML-driven changes in mass transport may lead to the clearance of proinflammatory factors, and this may cause the reduction in neutrophils observed with ML treatment.

The findings from this study suggest that there is an association between timely presence of neutrophils and ML-mediated improvements in functional recovery of injured muscle. Neutrophils have well-established tissue destructive and reparative roles via production of proteolytic enzymes, antimicrobial proteins, and reactive oxygen species, in addition to their phagocytotic and proangiogenic activity (*22*) (*36*–*41*). Contradictory results regarding the effects of neutrophil depletion on tissue regeneration have been previously reported, and the role of neutrophils likely depends on the timing of depletion, type of injury, and specific tissue/organ system (*38*, *39*) (*42*–*44*). The results of our studies highlight the importance of temporal aspects of neutrophil function in muscle after injury. Neutrophils play an important initial role in clearing dead cells and debris, as supported by the finding that their depletion before injury

in a similar model detrimentally affected regeneration (*45*). However, their long-term presence appears to impede muscle regeneration, as supported by previous work in which neutrophil depletion enhanced regeneration in a mild injury model where their phagocytotic function would not be essential (*44*). We also demonstrated that neutrophil-mediated factors stimulate the proliferation of MPCs but hamper their differentiation and the maturation of muscle fibers. The effects of neutrophil-secreted factors on myogenesis have not been previously identified, although a previous in vitro study implicated elastase secreted from neutrophils in diminished survival and differentiation of muscle cells in the context of muscular dystrophy (*40*). On a related note, previous studies have shown that early administration of nonsteroidal anti-inflammatory drugs after injury compromises skeletal muscle regeneration by hindering muscle stem cell expansion (*6*, *46*, *47*), supporting the importance of early inflammatory signaling for proper regeneration. Resolution of inflammation is equally important to enable completion of regenerative processes (*48*, *49*).

Among the factors that overlap between cytokines that were significantly decreased by ML in vivo and the major neutrophil-secreted factors, we identified Ccl3 and Mmp-9 as playing important roles in the proliferation and differentiation of MPCs. Little is known about the direct role of Ccl3 on primary MPC behaviors; however, it has been shown that supplementation of Ccl3 to culture medium increases proliferation of C2C12 myoblasts (*50*). Inhibition of Mmp-9 has been reported to improve proliferation and differentiation of MPCs in dystrophic muscle, and its temporal decrease may be critical to promoting skeletal muscle regeneration (*51*, *52*). Given that Ccl3 and Mmp-9 are also secreted by other immune and stromal cells and may exhibit divergent functions (*53*–*55*), their effects may be context dependent. Our studies focused on the effects of ML on muscle and immune cells, but the biology of various stromal cells is also likely an important contributor to muscle regeneration (*56*–*61*).

The mechanotransduction signaling pathway MRTF-A is a well-known regulator of muscle regeneration that stimulates MyoD-mediated myogenesis (*23*). In our system, Mrtf-a expression was increased with injury regardless of ML, but the $MyoD^+$ cell population was increased only with ML. There is a possibility that other mechanically activated regulators (i.e., YAP/TAZ, PIEZO I) can be associated with ML-mediated changes (*62*, *63*). Along with improved early myogenesis, ML induces the conversion of muscle fiber type composition similar to that found in healthy muscle at the later stage of regeneration, and the expression of *Pgc-1α*, a regulator of mitochondria biogenesis and muscle fiber conversion. The ML-mediated rapid reduction in proinflammatory cytokines (e.g., Tnf-α and Il-6) possibly dampens *Nf-κb* signaling pathways, which consequently stimulates up-regulation of *Pgc-1α* (*25*, *64*). A similar trend was found in a human study using massage therapy after exercise-mediated fatigue (*11*). Further analysis on splice variants of Pgc-1 in conjunction with specific fiber type formation in response to ML after severe injury will help elucidate a potential link between inflammation and fiber type plasticity during regeneration (*25*, *65*).

This study does have limitations. First, although we identified a therapeutic range of loading forces, the impact of other mechanical parameters (i.e., loading frequency, point of application, and number of cycles) remains to be explored. Although our study used a severe skeletal muscle injury model combining ischemic surgery with myotoxin injection, further studies with other clinically relevant injury models (e.g., volumetric muscle loss) will be important for future clinical translation. Third, although the study revealed that ML-mediated rapid clearance of neutrophiles improves muscle regeneration in part through enhancing early myogenesis, the mechanistic link to muscle fiber type transition at the later stages of regeneration requires further investigation.

As compared with drug- or biologic-based therapies commonly investigated in regenerative medicine, robotic-controlled and robotic-delivered ML has a lower barrier for translation to the clinic because of its noninvasive nature, ability to automate and personalize therapeutic delivery, and low burden of regulatory requirements. Although not directly assessed here, the noninvasive ML we used provided comparable therapeutic efficacy to pharmaceutical interventions (*5*), (*66*) and stem cell therapies in preclinical studies (*67*, *68*), and more consistent functional force restoration than implantation of acellular ECM (*7*, *69*, *70*). Although it will likely be necessary to optimize the loading treatment for specific types of injuries, regimens of ML may be beneficial for the regeneration of a wide array of tissue types, including bone, tendon, hair, and skin (*71*–*74*). Biologic-free and noninvasive approaches may also be beneficial for patients suffering from chronic inflammation, including idiopathic inflammatory myopathies, cancer-associated cachexia, and aging-associated sarcopenia. Immunosuppressant drugs are often ineffective in these patients, and physical therapy has been recommended as an alternative (*75*–*77*). There likely will also exist synergistic and/or antagonistic cross-talk between ML-based and biological agent–based therapies, and appropriate combinatorial therapeutic strategies may be effective (*71*, *78*).

MATERIALS AND METHODS

Study design

The aim of this study was to elucidate therapeutic loading conditions and the mechanisms underlying the effects of mechanotherapy for skeletal muscle regeneration. To this end, we developed a robotic actuation system, which allows measurement and control of the applied compressive loading. All animal work was performed in compliance with the National Institutes of Health (NIH) and institutional guidelines. For the mouse model of skeletal muscle injury, we strictly followed the protocol approved by the Institutional Animal Care and Use Committee at Harvard University. Briefly, 6- to 9-week-old female mice were subjected to a combination of intramuscular injection of myotoxin and induction of hindlimb ischemia. Mice were stratified according to severity of injury, and severely injured mice were selected and randomly assigned to different treatment groups. In general, experiments aimed to include five or more mice per group, and sample numbers for each individual experiment are provided in the figure legends. Functional outcomes were determined by assessing contractile forces and histological appearances of muscle 14 days after injury, unless otherwise noted. The molecular and cellular changes in injured muscle in response to ML were screened via immunoblotting, flow cytometry, immunofluorescence imaging, and RT-qPCR. In vitro myogenesis assay was performed with freshly isolated primary murine MPCs and neutrophils. Intramuscular neutrophils and macrophages were depleted with administration of an anti-Ly6g antibody and clodronate-containing liposome, respectively, to demonstrate their effects on skeletal muscle regeneration with ML. Histological assessments were performed in a blinded manner. All other analyses (cytokine array, Western blot, RT-qPCR, contractile force measurements, flow cytometry, and image analyses) were performed in an unbiased fashion. The individual

subject-level values, when *n* is smaller than 20, are included in data file S1.

Robotic actuator fabrication

Mechatronic muscle stimulating devices were developed to apply controlled and quantifiable forces to muscle tissues during in vivo testing. These devices use an electromagnetic linear actuator and force sensor assembly and use a force-control scheme that allows preprogrammed force profiles to be applied to muscle tissues (Fig. 1A). We used an electromechanical linear actuator (i) [19.1 mm (housing outer diameter), 44.5 mm (housing length), and 87.9 mm (total length)] (Moticont, DDLM-019-044-01) to provide the actuation force, and a load cell [18.5 mm (length), 5.59 mm (width), and 6.5 mm (depth) (Honeywell, FS010WNGX)] to provide feedback control. The force sensor was fabricated into a soft molded tip (ii) [19.1 mm (end diameter) and 4 mm (tip diameter)] (DragonSkin FX pro, SmoothOn) that applies cyclical loading to the tissue, allowing a measurement of the normal force being applied at a given instance. The positioning clamp (iii) helps to easily position the actuator toward the mouse limb. The mouse limb is restrained within a silicone-interfaced fixture (iv) [7.2 mm (inter diameter)] (DragonSkin FX pro, SmoothOn) that supports the reaction force on the mouse limb (Fig. 1A). The force signal measured by the force sensor is processed by an instrumentation amplifier (Honeywell, UV-10), and the signal is acquired by an analog input module (National Instruments, NI 9205). Using a real-time controller (National Instruments, cRIO-9030), a proportional-integral control algorithm, implemented on a field-programmable gate array, is used to regulate the force output according to a desired input force. The digital controller output signal is converted to an analog output using a digital-to-analog module (National Instruments, NI9264), and this signal is passed to a motor driver (MotiCont, 950 series), which supplies current to the electromechanical actuator. A host personal computer (PC) is used to issue commands to the real-time controller through a graphical user interface implemented on Labview (Labview, National Instruments). Controller gains and force commands can be passed from the host PC to the real-time controller. In addition, force sensing information in a graphical form can be relayed back to the host PC and recorded in synchrony with the force commands. Any arbitrary force profile can be programmed into the stimulating devices, and the frequency and amplitude of loading can also be varied. Devices were calibrated using a precision scale (Ohaus Scout). The stimulator assembly can be locked into position to ensure loading of the TA muscle in the normal direction. The adjustable clamp, which holds the actuator, allows the ultrasound transducer to easily maneuver for optimal imaging during muscle stimulation. In this study, we used the following parameters with this device: cyclic compression with square wave force profile, 1 Hz, and 20% (on)/80% (off) duty cycle. Magnitude of force was varied.

Skeletal muscle injury model and ML treatment

Skeletal muscle injury was induced in female C57BL6/J mice at 6 to 9 weeks of age (the Jackson Laboratory) by combination of snake venom toxin (notexin) injection with hindlimb ischemia. This injury model has been well established (*20*, *79*) and used as an experimental model of severe skeletal muscle injury because of the direct damage to muscle fibers and prolonged injury, in the absence of any defects in satellite cells or immune cells (*80*). All mice within each experiment were age matched, scored on the day of ischemic surgery in relation to the degree of myotoxin-mediated injury, and randomly distributed into experimental groups. Before toxin injection and surgical procedures, mice were anesthetized with an intraperitoneal injection of a mixture of ketamine (120 mg kg^{-1}) and xylazine (10 mg kg^{-1}). For toxin injection, 10 μl of notexin (10 μg/ml; Accurate Chemicals) was injected into the TA muscle upon anesthesia. After 6 days, hindlimb ischemia was induced on the same side of TA treated with notexin by unilateral ligation of the external iliac and femoral arteries and veins with 5-0 Ethilon sutures as previously described (*4*, *66*). Blood perfusion of ischemic limb relative to contralateral limb was measured using a laser Doppler perfusion imaging analyzer (PeriScan PIM II, Perimed AB) for confirmation of ischemic surgery as previously described (*4*). The next day, mice were randomized and divided into groups for the studies. For the ML group, mice were anesthetized with isofluorane during ML, whereas the untreated group of mice was placed in the isofluorane chamber to keep the amount of exposure to the anesthetic agent equivalent for both groups. The injured limb was placed on the limb restrainer, and the ankle was tied with a silicone cord to prevent any movement of the limb during treatment. The TA muscle in the limb was oriented to face the actuator horizontally. Each mouse was treated for 5 min every 10 to 12 hours. After the treatment, mice were returned to their cages. A previously developed pressure cuff was also used to apply ML in certain studies (*20*).

Cytokine screening analysis of TA muscle

To screen cytokine profiles, TA muscle was isolated from the mice with and without ML on days 3, 7, and 14 after ischemic surgery. Here, the ML was applied with our previous version of robotic actuator, a pressure cuff (*20*); analysis confirmed that both the pressure cuff and the current robotic device provided similar functional recovery of muscle regeneration (fig. S22). The isolated TA muscle was then minced and sonicated on ice, and tissue lysate was prepared in T-PER Tissue Protein Extraction Reagent (Thermo Fisher Scientific) containing protease and phosphatase inhibitors (Thermo Fisher Scientific). Tissue lysate was pooled from five samples per condition to obtain enough volume of concentrated lysate and normalized by muscle weight. The Proteome Profiler Mouse XL Cytokine Array (R&D) was used to assess the relative quantity of 111 different mouse cytokines and chemokines in TA muscle with and without ML (Table 1). Relative changes in array intensity for each cytokine from ML-treated group over untreated control group were calculated at days 3, 7, and 14 (D3, D7, and D14). For those cytokines whose intensity was weaker than the background signal (i.e., intensity value became negative), an arbitrary value of 0.1 was used to enable the calculation. The cytokines whose intensities were reduced by at least 50% with ML relative to the untreated group (the relative ratio of ML-treated group over control group <0.5) on day 3 were selected for further analysis. The selected factors were plotted with their relative quantity (ML over Ctrl) versus the day in a heatmap using the Python package Seaborn, and the top enriched Gene Ontology terms were found using the web tool ShinyGO v0.60 (http://bioinformatics.sdstate.edu/go/) and cross-checked with DAVID Bioinformatics and Resources 6.8 (https://david.ncifcrf.gov/summary.jsp). The results are listed in table S2.

Immune cell population analysis

To assess the changes in intramuscular immune cell populations, TA muscle was minced, digested using the skeletal muscle dissociation

kit (MACS Miltenyi Biotec) with the gentleMACS dissociator, and filtered through a 70-μm cell strainer to obtain a single-cell suspension. The isolated cells were blocked with CD16/CD32 monoclonal antibody (eBioscience) and then stained with the following antibodies: CD45–phycoerythrin (PE) or CD45-PerCP/Cyanine (Cy)5.5, Ly6C–Pacific Blue, T cell receptor (TCR)–PE/Cy7, CD86–fluorescein isothiocyanate (FITC), CD80–Pacific Blue (aforementioned antibodies from BioLegend), CD11c–anaphase-promoting complex (APC), CD11b-PE/Cy7, F4/80-PE or F4/80-PerCP/Cy5, Ly6G-FITC, CD206-APC, CD3–Pacific Blue, CD4-PE/Cy7, or CD4-PE (the rest from eBioscience) at the concentrations recommended by the manufacturers. Detailed information for antibodies is listed in table S3. Then, cells were stained with LIVE/DEAD Fixable near-infrared stain (Thermo Fisher Scientific), fixed with 0.4% paraformaldehyde, and stored at 4°C until they were assessed with an LSR II flow cytometer. Unstained cells, fluorescence minus one controls, and the appropriate isotype controls recommended by the manufacturers were used as controls in the gating. The following definitions were used to define the specific populations based on live cells: monocyte/macrophages ($CD45^+/CD11c^-/CD11b^+/F4/80^+/Ly6g^-$); M1 macrophages ($CD11b^+/F4/80^+/CD86^+/CD80^+$); M2 macrophages ($CD11b^+/F4/80^+/CD206^+$); dendritic cells ($CD45^+/CD11c^+/CD11b^+$); and T cells ($CD45^+/CD3^+/CD4^+$ or $CD45^+/TCR^+/CD4^+$, depending on staining panels). Neutrophils ($CD45^+/CD11c^-/CD11b^+/F4/80^-/Ly6g^+/Ly6c^{intermediate}$) were defined and gated as described in fig. S23. Immune cells from other organs such as spleen, lung, and bone marrow were similarly isolated, stained, and analyzed as described above. Spleen and bone marrow did not require digestion procedures, yet the lung dissociation kit (MACS Miltenyl Biotec) with the gentleMACS dissociator was used for proper digestion of lung tissue. For cytokine staining within neutrophils, the surface markers of neutrophils were stained first, and cells were fixed and permeabilized with Intracellular Fixation and Permeabilization Buffer set (eBioscience). Then, cells were stained with primary antibodies [Cxcl2 (Novus Biologicals) and Mmp-9 (Thermo Fisher Scientific)] followed by the respective secondary antibodies [APC-conjugated goat immunoglobulin G (IgG) antibody or PerCP/Cy5–conjugated mouse IgG 2b antibody], or APC-conjugated Interferon (Inf)-γ (BioLegend). Mean fluorescence intensity of Cxcl2, Mmp-9, and Inf-γ was measured among neutrophils ($CD45^+/CD11b^+/F4/80^-/Ly6g^+/Ly6c^{intermediate}$). Immunofluorescence staining of immune cell markers was performed following the standard protocol used for Pax7 and desmin (both from Abcam). The following primary antibodies were used: Ly6g (BioLegend), myeloperoxidase (Bosterbio), CD68 (Abcam), and CCR7 (Abcam).

In vitro assays of primary MPC proliferation and differentiation

MPCs were isolated from the hindlimb muscles of 6- to 9-week-old female C57BL6/J mice, which were injected with 1.2% barium chloride ($BaCl_2$) 4 days before isolation. Hindlimb muscles were isolated under sterile conditions, minced, digested, and filtered through a 70-μm cell strainer to obtain a single-cell suspension as previously described (*4*, *5*). The mouse satellite cell isolation kit (Miltenyi Biotec) was applied to the cell suspension to select a cell population enriched with satellite cells or MPCs. The resulting cell population was cultured and expanded on collagen-coated dishes (Corning) for 6 to 8 days in F10 media (Gibco), supplemented with 20% fetal bovine serum (FBS; Gibco), 1% penicillin-streptomycin (P/S; Gibco), and basic fibroblast growth factor (bFGF; 50 ng/ml; PeproTech). After the culture, only loosely adherent MPCs were lifted and collected by treatment with phosphate-buffered saline (PBS) for 10 min at 37°C while leaving behind strongly adherent fibroblasts. MPCs were then seeded on an eight-well, collagen I–coated multiwell culture slide (Corning) at 6000 or 30,000 cells per well in F10 media (20% FBS, 1% P/S) for proliferation or differentiation, respectively. After allowing cells to adhere for 24 hours, cells were rinsed with serum-free F10 media and then cultured with a 1:1 mixture of F10 media (2% FBS, 1% P/S) with NeutCM for 3 days for proliferation studies, and a 1:1 mixture of Dulbecco's modified Eagle medium (5% horse serum, 1% P/S) with NeutCM for 5-day differentiation studies. As a control, NeutCM control media was prepared in the same manner, although without neutrophil culture. To analyze proliferation, the thymidine analog 5-ethynyl-2′-deoxyuridine (EdU) was added into the culture media on day 3, incubated for 18 hours, and cells were fixed and stained with Click-iT EdU Alexa Fluor 555 Imaging Kit (Invitrogen) according to the manufacturer's protocol. The number of EdU-incorporated satellite cells was counted and normalized by the total number of cells stained with Pax7, MyHC, and 4′,6-diamidino-2-phenylindole (DAPI). For analysis of differentiation, satellite cells were fixed and stained for MyHC and desmin. The fixed samples were blocked with 3% bovine serum albumin (Sigma-Aldrich) in PBS and M.O.M. (Mouse on Mouse) Blocking Reagent (Vector Laboratories) and incubated with primary antibodies [rabbit anti-Pax7 (Abcam), mouse anti-MyHC (R&D), and rabbit anti-desmin (Abcam)] overnight at 4°C. The next day, the samples were washed and stained with secondary antibodies [anti-rabbit Alexa Fluor 568 and anti-mouse Alexa Fluor 647 (Thermo Fisher Scientific)]. The number and length of MyHC and desmin-positive multinuclei myotubes were analyzed using Image J.

Neutrophil recruitment inhibition in vivo

Skeletal muscle injury was induced in 6- to 9-week-old female C57BL6/J mice as described above. The mice were randomized after ischemic surgery and divided into four groups: (i) untreated control, (ii) ML-treated group, (iii) anti-Ly6g antibody–treated group, and (iv) its control IgG antibody–treated group. For antibody-treated groups, 100 μl of monoclonal anti-mouse Ly6g antibody [clone 1A8 (Bio X Cell) or its control IgG antibody (Bio X Cell)] reconstituted in PBS was intravenously administered at the concentration of 5 mg/ml once a day for the first 3 days after surgery. A day after administration of anti-Ly6g antibody, the number of systemic neutrophils detected by Ly6G antibody was assessed before the study (fig. S24). The ML-treated group received ML as described above. After 14 days, the TA muscle was isolated for the analysis of functional tetanic forces and histological features.

RNA extraction and RT-qPCR

Total RNA was extracted from muscle tissues using the Aurum total RNA fatty and fibrous tissues kit (Bio-Rad) and following the manufacturer's instructions. Primers used for this study were designed using Primer Blast (NIH) and manufactured by Sigma-Aldrich. A list of primers sequences is included in table S4. Additional details are provided in the Supplementary Materials.

Statistical analysis

GraphPad Prism 6 was used to perform statistical analysis. First, the normality of samples was checked with the Shapiro-Wilk tests.

For normally distributed samples, Student's *t* tests and analysis of variance (ANOVA) were used to compare parametric data between two conditions and among multiple conditions, respectively. For ANOVA, post hoc pairwise comparisons were determined by Tukey's test. For nonparametric or not-normally distributed data, Mann-Whitney *U* and Kruskal-Wallis tests with Dunn's post hoc tests were used to compare two groups or multiple groups, respectively. Two-way ANOVA followed by Bonferroni's test was used when two independent variables exist. For RT-qPCR data, depending on the homogeneity of variance, either one-way ANOVA with Tukey post hoc test or Welch ANOVA with Games Howell was used. Two-sided testing was performed for each analysis, and $P < 0.05$ was considered statistically significant. Unless otherwise noted, values are reported as the means with error bars to indicate SDs, and the results are compiled from separate replicate experiments.

SUPPLEMENTARY MATERIALS

www.science.org/doi/10.1126/scitranslmed.abe8868
Materials and methods
Figs. S1 to S24
Tables S1 to S4
Movies S1 and S2
Data file S1
References (*81*–*86*)

View/request a protocol for this paper from *Bio-protocol*.

REFERENCES AND NOTES

1. J. Liu, D. Saul, K. O. Böker, J. Ernst, W. Lehman, A. F. Schilling, Current methods for skeletal muscle tissue repair and regeneration. *Biomed. Res. Int.* **2018**, 1984879 (2018).
2. N. J. Turner, S. F. Badylak, Regeneration of skeletal muscle. *Cell Tissue Res.* **347**, 759–774 (2012).
3. J. G. Tidball, Regulation of muscle growth and regeneration by the immune system. *Nat. Rev. Immunol.* **17**, 165–178 (2017).
4. B. J. Kwee, B. R. Seo, A. J. Najibi, A. W. Li, T.-Y. Shih, D. White, D. J. Mooney, Treating ischemia via recruitment of antigen-specific T cells. *Sci. Adv.* **5**, eaav6313 (2019).
5. T. M. Raimondo, D. J. Mooney, Functional muscle recovery with nanoparticle-directed M2 macrophage polarization in mice. *Proc. Natl. Acad. Sci. U.S.A.* **115**, 10648–10653 (2018).
6. A. T. V. Ho, A. R. Palla, M. R. Blake, N. D. Yucel, Y. X. Wang, K. E. G. Magnusson, C. A. Holbrook, P. E. Kraft, S. L. Delp, H. M. Blau, Prostaglandin E2 is essential for efficacious skeletal muscle stem-cell function, augmenting regeneration and strength. *Proc. Natl. Acad. Sci. U.S.A.* **114**, 6675–6684 (2017).
7. B. M. Sicari, J. P. Rubin, C. L. Dearth, M. T. Wolf, F. Ambrosio, M. Boninger, N. J. Turner, D. J. Weber, T. W. Simpson, A. Wyse, E. H. Brown, J. L. Dziki, L. E. Fisher, S. Brown, S. F. Badylak, An acellular biologic scaffold promotes skeletal muscle formation in mice and humans with volumetric muscle loss. *Sci. Transl. Med.* **6**, 234ra258 (2014).
8. K. Sadtler, K. Estrellas, B. W. Allen, M. T. Wolf, H. Fan, A. J. Tam, C. H. Patel, B. S. Luber, H. Wang, K. R. Wagner, J. D. Powell, F. Housseau, D. M. Pardoll, J. H. Elisseeff, Developing a pro-regenerative biomaterial scaffold microenvironment requires T helper 2 cells. *Science* **352**, 366–370 (2016).
9. N. J. Willett, M. L. Boninger, L. J. Miller, L. Alvarez, T. Aoyama, M. Bedoni, K. A. Brix, C. Chisari, G. Christ, C. L. Dearth, T. A. Dyson-Hudson, C. H. Evans, S. M. Goldman, K. Gregory, A. Gualerzi, J. Hart, A. Ito, H. Kuroki, M. T. Loghmani, D. L. Mack, G. A. Malanga, L. Noble-Haeusslein, P. Pasquina, J. A. Roche, L. Rose, M. J. Stoddart, J. Tajino, C. Terzic, K. S. Topp, W. R. Wagner, S. J. Warden, S. L. Wolf, H. Xie, T. A. Rando, F. Ambrosio, Taking the next steps in regenerative rehabilitation: Establishment of a new interdisciplinary field. *Arch. Phys. Med. Rehabil.* **101**, 917–923 (2020).
10. H. Mori, H. Ohsawa, T. H. Tanaka, E. Taniwaki, G. Leisman, K. Nishijo, Effect of massage on blood flow and muscle fatigue following isometric lumbar exercise. *Med. Sci. Monit.* **10**, CR173–CR178 (2004).
11. J. D. Crane, D. I. Ogborn, C. Cupido, S. Melov, A. Hubbard, J. M. Bourgeois, M. A. Tarnopolsky, Massage therapy attenuates inflammatory signaling after exercise-induced muscle damage. *Sci. Transl. Med.* **4**, 119ra113 (2012).
12. C. Waters-Banker, T. A. Butterfield, E. E. Dupont-Versteegden, Immunomodulatory effects of massage on nonperturbed skeletal muscle in rats. *J. Appl. Physiol. (1985)* **116**, 164–175 (2014).
13. G. Giatsidis, L. Cheng, A. Haddad, K. Ji, J. Succar, L. Lancerotto, J. Lujan-Hernandez, P. Fiorina, H. Matsumine, D. P. Orgill, Noninvasive induction of angiogenesis in tissues by external suction: Sequential optimization for use in reconstructive surgery. *Angiogenesis* **21**, 61–78 (2018).
14. C. K. Sen, S. Khanna, H. Harris, R. Stewart, M. Balch, M. Heigel, S. Teplitsky, S. Gnyawali, C. Rink, Robot-assisted mechanical therapy attenuates stroke-induced limb skeletal muscle injury. *FASEB J.* **31**, 927–936 (2017).
15. J. S. You, R. M. McNally, B. L. Jacobs, R. E. Privett, D. M. Gundermann, K. H. Lin, N. D. Steinert, C. A. Goodman, T. A. Hornberger, The role of raptor in the mechanical load-induced regulation of mTOR signaling, protein synthesis, and skeletal muscle hypertrophy. *FASEB J.* **33**, 4021–4034 (2019).
16. C. Haas, T. A. Butterfield, S. Abshire, Y. Zhao, X. Zhang, D. Jarjoura, T. M. Best, Massage timing affects postexercise muscle recovery and inflammation in a rabbit model. *Med. Sci. Sports Exerc.* **45**, 1105–1112 (2013).
17. D. D. Damian, K. Price, S. Arabagi, I. Berra, Z. Machaidze, S. Manjila, S. Shimada, A. Fabozzo, G. Arnal, D. Van Story, J. D. Goldsmith, A. T. Agoston, C. Kim, R. W. Jennings, P. D. Ngo, M. Manfredi, P. E. Dupont, In vivo tissue regeneration with robotic implants. *Sci. Robot.* **3**, eaaq0018 (2018).
18. E. B. Dolan, C. E. Varela, K. Mendez, W. Whyte, R. E. Levey, S. T. Robinson, E. Maye, J. O'Dwyer, R. Beatty, A. Rothman, Y. Fan, J. Hochstein, S. E. Rothenbucher, R. Wylie, J. R. Starr, M. Monaghan, P. Dockery, G. P. Duffy, E. T. Roche, An actuatable soft reservoir modulates host foreign body response. *Sci. Robot.* **4**, eaax7043 (2019).
19. Y. Wang, J. Song, X. Liu, J. Liu, Q. Zhang, X. Yan, X. Yuan, D. Ren, Multiple effects of mechanical stretch on myogenic progenitor cells. *Stem Cells Dev.* **29**, 336–352 (2020).
20. C. A. Cezar, E. T. Roche, H. H. Vandenburgh, G. N. Duda, C. J. Walsh, D. J. Mooney, Biologic-free mechanically induced muscle regeneration. *Proc. Natl. Acad. Sci. U.S.A.* **113**, 1534–1539 (2016).
21. K. M. Wisdom, S. L. Delp, E. Kuhl, Use it or lose it: Multiscale skeletal muscle adaptation to mechanical stimuli. *Biomech. Model. Mechanobiol.* **14**, 195–215 (2015).
22. M. Peiseler, P. Kubes, More friend than foe: The emerging role of neutrophils in tissue repair. *J. Clin. Invest.* **129**, 2629–2639 (2019).
23. M. H. Mokalled, A. N. Johnson, E. E. Creemers, E. N. Olson, MASTR directs MyoD-dependent satellite cell differentiation during skeletal muscle regeneration. *Genes Dev.* **26**, 190–202 (2012).
24. B. K. Cenik, N. Liu, B. Chen, S. Bezprozvannaya, E. N. Olson, R. Bassel-Duby, Myocardin-related transcription factors are required for skeletal muscle development. *Development* **143**, 2853–2861 (2016).
25. C. Handschin, B. M. Spiegelman, The role of exercise and PGC1alpha in inflammation and chronic disease. *Nature* **454**, 463–469 (2008).
26. S. Schiaffino, C. Reggiani, Fiber types in mammalian skeletal muscles. *Physiol. Rev.* **91**, 1447–1531 (2011).
27. M. Kammoun, I. Cassar-Malek, B. Meunier, B. Picard, A simplified immunohistochemical classification of skeletal muscle fibres in mouse. *Eur. J. Histochem.* **58**, 2254 (2014).
28. Z. Arany, N. Lebrasseur, C. Morris, E. Smith, W. Yang, Y. Ma, S. Chin, B. M. Spiegelman, The transcriptional coactivator PGC-1beta drives the formation of oxidative type IIX fibers in skeletal muscle. *Cell Metab.* **5**, 35–46 (2007).
29. J. Lin, H. Wu, P. T. Tarr, C. Y. Zhang, Z. Wu, O. Boss, L. F. Michael, P. Puigserver, E. Isotani, E. N. Olson, B. B. Lowell, R. Bassel-Duby, B. M. Spiegelman, Transcriptional co-activator PGC-1 alpha drives the formation of slow-twitch muscle fibres. *Nature* **418**, 797–801 (2002).
30. P. S. Eisele, S. Salatino, J. Sobek, M. O. Hottiger, C. Handschin, The peroxisome proliferator-activated receptor γ coactivator 1α/β (PGC-1) coactivators repress the transcriptional activity of NF-κB in skeletal muscle cells. *J. Biol. Chem.* **288**, 2246–2260 (2013).
31. D. Alvarez-Guardia, X. Palomer, T. Coll, M. M. Davidson, T. O. Chan, A. M. Feldman, J. C. Laguna, M. Vazquez-Carrera, The p65 subunit of NF-kappaB binds to PGC-1alpha, linking inflammation and metabolic disturbances in cardiac cells. *Cardiovasc. Res.* **87**, 449–458 (2010).
32. G. C. Rowe, I. S. Patten, Z. K. Zsengeller, R. El-Khoury, M. Okutsu, S. Bampoh, N. Koulisis, C. Farrell, M. F. Hirshman, Z. Yan, L. J. Goodyear, P. Rustin, Z. Arany, Disconnecting mitochondrial content from respiratory chain capacity in PGC-1-deficient skeletal muscle. *Cell Rep.* **3**, 1449–1456 (2013).
33. V. Ballotta, A. Driessen-Mol, C. V. Bouten, F. P. Baaijens, Strain-dependent modulation of macrophage polarization within scaffolds. *Biomaterials* **35**, 4919–4928 (2014).
34. E. G. Hevia, N. Phipps, C. J. Payne, A. Atalay, O. Atalay, B. R. Seo, D. J. Mooney, C. Walsh, Force control of textile-based soft wearable robots for mechanotherapy. *IEEE Int. Conf. Robot. Autom.* **2018**, 5459–5465 (2018).
35. C. J. P. V. Sanchez, D. J. Preston, J. T. Alvarez, J. C. Weaver, A. T. Atalay, M. Boyvat, D. M. Vogt, R. J. Wood, G. M. Whitesides, C. J. Walsh, Smart thermally actuating textiles. *Adv. Mater. Technol.* **5**, 2000383 (2020).
36. T. J. McLoughlin, S. K. Tsivitse, J. A. Edwards, B. A. Aiken, F. X. Pizza, Deferoxamine reduces and nitric oxide synthase inhibition increases neutrophil-mediated myotube injury. *Cell Tissue Res.* **313**, 313–319 (2003).

37. H. X. Nguyen, J. G. Tidball, Null mutation of gp91phox reduces muscle membrane lysis during muscle inflammation in mice. *J. Physiol.* **553**, 833–841 (2003).
38. S. Brickson, L. L. Ji, K. Schell, R. Olabisi, B. St Pierre Schneider, T. M. Best, M1/70 attenuates blood-borne neutrophil oxidants, activation, and myofiber damage following stretch injury. *J. Appl. Physiol. (1985)* **95**, 969–976 (2003).
39. J. N. Crinnion, S. Homer-Vanniasinkam, R. Hatton, S. M. Parkin, M. J. Gough, Role of neutrophil depletion and elastase inhibition in modifying skeletal muscle reperfusion injury. *Cardiovasc. Surg.* **2**, 749–753 (1994).
40. N. Arecco, C. J. Clarke, F. K. Jones, D. M. Simpson, D. Mason, R. J. Beynon, A. Pisconti, Elastase levels and activity are increased in dystrophic muscle and impair myoblast cell survival, proliferation and differentiation. *Sci. Rep.* **6**, 24708 (2016).
41. J. Frenette, B. Cai, J. G. Tidball, Complement activation promotes muscle inflammation during modified muscle use. *Am. J. Pathol.* **156**, 2103–2110 (2000).
42. W. Yang, Y. Tao, Y. Wu, X. Zhao, W. Ye, D. Zhao, L. Fu, C. Tian, J. Yang, F. He, L. Tang, Neutrophils promote the development of reparative macrophages mediated by ROS to orchestrate liver repair. *Nat. Commun.* **10**, 1076 (2019).
43. N. Nishio, Y. Okawa, H. Sakurai, K. Isobe, Neutrophil depletion delays wound repair in aged mice. *Age* **30**, 11–19 (2008).
44. F. X. Pizza, J. M. Peterson, J. H. Baas, T. J. Koh, Neutrophils contribute to muscle injury and impair its resolution after lengthening contractions in mice. *J. Physiol.* **562**, 899–913 (2005).
45. C. F. Teixeira, S. R. Zamunér, J. P. Zuliani, C. M. Fernandes, M. A. Cruz-Hofling, I. Fernandes, F. Chaves, J. M. Gutiérrez, Neutrophils do not contribute to local tissue damage, but play a key role in skeletal muscle regeneration, in mice injected with Bothrops asper snake venom. *Muscle Nerve* **28**, 449–459 (2003).
46. U. R. Mikkelsen, H. Langberg, I. C. Helmark, D. Skovgaard, L. L. Andersen, M. Kjaer, A. L. Mackey, Local NSAID infusion inhibits satellite cell proliferation in human skeletal muscle after eccentric exercise. *J. Appl. Physiol. (1985)* **107**, 1600–1611 (2009).
47. S. T. Mills, A. Bondesen, K. M. Kegley, G. K. Pavlath, The COX-2 pathway is essential during early stages of skeletal muscle regeneration. *Am. J. Physiol. Cell Physiol.* **287**, C475–C483 (2004).
48. L. Arnold, A. Henry, F. Poron, Y. Baba-Amer, N. van Rooijen, A. Plonquet, R. K. Gherardi, B. Chazaud, Inflammatory monocytes recruited after skeletal muscle injury switch into antiinflammatory macrophages to support myogenesis. *J. Exp. Med.* **204**, 1057–1069 (2007).
49. S. McArthur, G. Juban, T. Gobbetti, T. Desgeorges, M. Theret, J. Gondin, J. E. Toller-Kawahisa, C. P. Reutelingsperger, B. Chazaud, M. Perretti, R. Mounier, Annexin A1 drives macrophage skewing to accelerate muscle regeneration through AMPK activation. *J. Clin. Invest.* **130**, 1156–1167 (2020).
50. L. Yahiaoui, D. Gvozdic, G. Danialou, M. Mack, B. J. Petrof, CC family chemokines directly regulate myoblast responses to skeletal muscle injury. *J. Physiol.* **586**, 3991–4004 (2008).
51. N. Shiba, D. Miyazaki, T. Yoshizawa, K. Fukushima, Y. Shiba, Y. Inaba, M. Imamura, S. Takeda, K. Koike, A. Nakamura, Differential roles of MMP-9 in early and late stages of dystrophic muscles in a mouse model of Duchenne muscular dystrophy. *Biochim. Biophys. Acta* **1852**, 2170–2182 (2015).
52. S. M. Hindi, J. Shin, Y. Ogura, H. Li, A. Kumar, Matrix metalloproteinase-9 inhibition improves proliferation and engraftment of myogenic cells in dystrophic muscle of mdx mice. *PLOS ONE* **8**, e72121 (2013).
53. X. Chen, Y. Li, Role of matrix metalloproteinases in skeletal muscle: Migration, differentiation, regeneration and fibrosis. *Cell Adh. Migr.* **3**, 337–341 (2009).
54. R. J. Staversky, D. K. Byun, M. A. Georger, B. J. Zaffuto, A. Goodman, M. W. Becker, L. M. Calvi, B. J. Frisch, The Chemokine CCL3 regulates myeloid differentiation and hematopoietic stem cell numbers. *Sci. Rep.* **8**, 14691 (2018).
55. I. Bhavsar, C. S. Miller, M. Al-Sabbagh, Macrophage inflammatory protein-1 Alpha (MIP-1 alpha)/CCL3: As a biomarker. *General Methods Biomarker Res. App.* 223–249 (2015).
56. J. E. Heredia, L. Mukundan, F. M. Chen, A. A. Mueller, R. C. Deo, R. M. Locksley, T. A. Rando, A. Chawla, Type 2 innate signals stimulate fibro/adipogenic progenitors to facilitate muscle regeneration. *Cell* **153**, 376–388 (2013).
57. F. D. Camargo, R. Green, Y. Capetanaki, K. A. Jackson, M. A. Goodell, Single hematopoietic stem cells generate skeletal muscle through myeloid intermediates. *Nat. Med.* **9**, 1520–1527 (2003).
58. R. N. Judson, R.-H. Zhang, F. M. Rossi, Tissue-resident mesenchymal stem/progenitor cells in skeletal muscle: Collaborators or saboteurs? *FEBS J.* **280**, 4100–4108 (2013).
59. D. R. Lemos, F. Babaeijandaghi, M. Low, C.-K. Chang, S. T. Lee, D. Fiore, R.-H. Zhang, A. Natarajan, S. A. Nedospasov, F. M. Rossi, Nilotinib reduces muscle fibrosis in chronic muscle injury by promoting TNF-mediated apoptosis of fibro/adipogenic progenitors. *Nat. Med.* **21**, 786–794 (2015).
60. A. W. Joe, L. Yi, A. Natarajan, F. Le Grand, L. So, J. Wang, M. A. Rudnicki, F. M. Rossi, Muscle injury activates resident fibro/adipogenic progenitors that facilitate myogenesis. *Nat. Cell Biol.* **12**, 153–163 (2010).
61. B. Malecova, S. Gatto, U. Etxaniz, M. Passafaro, A. Cortez, C. Nicoletti, L. Giordani, A. Torcinaro, M. De Bardi, S. Bicciato, F. De Santa, L. Madaro, P. L. Puri, Dynamics of cellular states of fibro-adipogenic progenitors during myogenesis and muscular dystrophy. *Nat. Commun.* **9**, 3670 (2018).
62. J. S. Silver, K. A. Gunay, A. A. Cutler, T. O. Vogler, T. E. Brown, B. T. Pawlikowski, O. J. Bednarski, K. L. Bannister, C. J. Rogowski, A. G. McKay, F. W. DelRio, B. B. Olwin, K. S. Anseth, Injury-mediated stiffening persistently activates muscle stem cells through YAP and TAZ mechanotransduction. *Sci. Adv.* **7**, (2021).
63. K. Hirano, M. Tsuchiya, S. Takabayashi, K. Nagao, Y. Kitajima, Y. Ono, K. Nonomura, Y. Mori, M. Umeda, Y. Hara, The mechanosensitive Ca^{2+}-permeable ion channel PIEZO1 promotes satellite cell function in skeletal muscle regeneration. *BioRxiv* 10.1101/2021.03.18.435982 (2021).
64. X. Palomer, D. Alvarez-Guardia, R. Rodriguez-Calvo, T. Coll, J. C. Laguna, M. M. Davidson, T. O. Chan, A. M. Feldman, M. Vazquez-Carrera, TNF-alpha reduces PGC-1alpha expression through NF-kappaB and p38 MAPK leading to increased glucose oxidation in a human cardiac cell model. *Cardiovasc. Res.* **81**, 703–712 (2009).
65. M. Ydfors, H. Fischer, H. Mascher, E. Blomstrand, J. Norrbom, T. Gustafsson, The truncated splice variants, NT-PGC-1αandPGC-1α4, increase with both endurance and resistance exercise in human skeletal muscle. *Physiol. Rep.* **1**, e00140 (2013).
66. C. Borselli, H. Storrie, F. Benesch-Lee, D. Shvartsman, C. Cezar, J. W. Lichtman, H. H. Vandenburgh, D. J. Mooney, Functional muscle regeneration with combined delivery of angiogenesis and myogenesis factors. *Proc. Natl. Acad. Sci. U.S.A.* **107**, 3287–3292 (2010).
67. M. Quarta, M. Cromie, R. Chacon, J. Blonigan, V. Garcia, I. Akimenko, M. Hamer, P. Paine, M. Stok, J. B. Shrager, T. A. Rando, Bioengineered constructs combined with exercise enhance stem cell-mediated treatment of volumetric muscle loss. *Nat. Commun.* **8**, 15613 (2017).
68. A. Gorecka, S. Salemi, D. Haralampieva, F. Moalli, D. Stroka, D. Candinas, D. Eberli, L. Brugger, Autologous transplantation of adipose-derived stem cells improves functional recovery of skeletal muscle without direct participation in new myofiber formation. *Stem Cell Res. Ther.* **9**, 195 (2018).
69. A. Aurora, J. L. Roe, B. T. Corona, T. J. Walters, An acellular biologic scaffold does not regenerate appreciable de novo muscle tissue in rat models of volumetric muscle loss injury. *Biomaterials* **67**, 393–407 (2015).
70. A. Urciuolo, L. Urbani, S. Perin, P. Maghsoudlou, F. Scottoni, A. Gjinovci, H. Collins-Hooper, S. Loukogeorgakis, A. Tyraskis, S. Torelli, E. Germinario, M. E. A. Fallas, C. Julia-Vilella, S. Eaton, B. Blaauw, K. Patel, P. De Coppi, Decellularised skeletal muscles allow functional muscle regeneration by promoting host cell migration. *Sci. Rep.* **8**, 8398 (2018).
71. A. Iura, E. G. McNerny, Y. Zhang, N. Kamiya, M. Tantillo, M. Lynch, D. H. Kohn, Y. Mishina, Mechanical loading synergistically increases trabecular bone volume and improves mechanical properties in the mouse when BMP signaling is specifically ablated in osteoblasts. *PLOS ONE* **10**, e0141345 (2015).
72. S. Y. Chu, C. H. Chou, H. D. Huang, M. H. Yen, H. C. Hong, P. H. Chao, Y. H. Wang, P. Y. Chen, S. X. Nian, Y. R. Chen, L. Y. Liou, Y. C. Liu, H. M. Chen, F. M. Lin, Y. T. Chang, C. C. Chen, O. K. Lee, Mechanical stretch induces hair regeneration through the alternative activation of macrophages. *Nat. Commun.* **10**, 1524 (2019).
73. S. O. Blacklow, J. Li, B. R. Freedman, M. Zeidi, C. Chen, D. J. Mooney, Bioinspired mechanically active adhesive dressings to accelerate wound closure. *Sci. Adv.* **5**, eaaw3963 (2019).
74. B. R. Freedman, A. B. Rodriguez, R. J. Leiphart, J. B. Newton, E. Ban, J. J. Sarver, R. L. Mauck, V. B. Shenoy, L. J. Soslowsky, Dynamic loading and tendon healing affect multiscale tendon properties and ECM stress transmission. *Sci. Rep.* **8**, 10854 (2018).
75. J. Schmidt, Current classification and management of inflammatory myopathies. *J. Neuromuscul. Dis.* **5**, 109–129 (2018).
76. T. Aoyagi, K. P. Terracina, A. Raza, H. Matsubara, K. Takabe, Cancer cachexia, mechanism and treatment. *World J. Gastrointest. Oncol.* **7**, 17–29 (2015).
77. S. Dalle, L. Rossmeislova, K. Koppo, The role of inflammation in age-related sarcopenia. *Front. Physiol.* **8**, 1045 (2017).
78. B. Christensen, S. Dandanell, M. Kjaer, H. Langberg, Effect of anti-inflammatory medication on the running-induced rise in patella tendon collagen synthesis in humans. *J. Appl. Physiol. (1985)* **110**, 137–141 (2011).
79. L. Wang, L. Cao, J. Shansky, Z. Wang, D. Mooney, H. Vandenburgh, Minimally invasive approach to the repair of injured skeletal muscle with a shape-memory scaffold. *Mol. Ther.* **22**, 1441–1449 (2014).
80. D. Hardy, A. Besnard, M. Latil, G. Jouvion, D. Briand, C. Thepenier, Q. Pascal, A. Guguin, B. Gayraud-Morel, J. M. Cavaillon, S. Tajbakhsh, P. Rocheteau, F. Chretien, Comparative study of injury models for studying muscle regeneration in mice. *PLOS ONE* **11**, e0147198 (2016).
81. C. F. Guimarães, L. Gasperini, A. P. Marques, R. L. Reis, The stiffness of living tissues and its implications for tissue engineering. *Nat. Rev. Mater.* **5**, 351–370 (2020).
82. O. Chaudhuri, L. Gu, D. Klumpers, M. Darnell, S. A. Bencherif, J. C. Weaver, N. Huebsch, H. P. Lee, E. Lippens, G. N. Duda, D. J. Mooney, Hydrogels with tunable stress relaxation regulate stem cell fate and activity. *Nat. Mater.* **15**, 326–334 (2016).

83. M. O. Dellacherie, A. Li, B. Y. Lu, C. S. Verbeke, L. Gu, A. G. Stafford, E. J. Doherty, D. J. Mooney, Single-shot mesoporous silica rods scaffold for induction of humoral responses against small antigens. *Adv. Funct. Mater.* **30**, 2002448 (2020).
84. L. Encarnacion-Rivera, S. Foltz, H. C. Hartzell, H. Choo, Myosoft: An automated muscle histology analysis tool using machine learning algorithm utilizing FIJI/ImageJ software. *PLOS ONE* **15**, e0229041 (2020).
85. B. R. Seo, P. Bhardwaj, S. Choi, J. Gonzalez, R. C. Andresen Eguiluz, K. Wang, S. Mohanan, P. G. Morris, B. Du, X. K. Zhou, L. T. Vahdat, A. Verma, O. Elemento, C. A. Hudis, R. M. Williams, D. Gourdon, A. J. Dannenberg, C. Fischbach, Obesity-dependent changes in interstitial ECM mechanics promote breast tumorigenesis. *Sci. Transl. Med.* **7**, 301ra130 (2015).
86. K. J. Livak, T. D. Schmittgen, Analysis of relative gene expression data using real-time quantitative PCR and the 2(-Delta Delta C(T)) method. *Methods* **25**, 402–408 (2001).

Acknowledgments: We acknowledge C. Cezar for the helpful discussion and C. Hellriegel and E. Diel for assistance at the Harvard Center for Biological Imaging. We thank T. Ferrante for help with confocal imaging at Wyss Institute. We also thank R. Bronson of the Harvard Rodent Histopathology Core for the assessment of histology sections and acknowledge the Dana-Farber/Harvard Cancer Center in Boston, MA, for the use of the Rodent Histopathology Core. The Dana-Farber/Harvard Cancer Center is supported in part by an NCI Cancer Center Support Grant no. NIH 5 P30 CA06516. We acknowledge Z. Niziolek and J. Nelson at the Bauer Core Facility at Harvard for help with flow cytometry. We also acknowledge L. Encarnacion-Rivera at Stanford University for help with Myosoft. **Funding:** Research reported in this publication was supported by the National Institute of Dental and Craniofacial Research under award number R01DE013349 (D.J.M.) and the Eunice Kennedy Shriver National Institute of Child Health and Human Development under award number P2CHD086843 (D.J.M.). We also acknowledge support from the Materials and Research Science and Engineering Centers (MRSEC) grant award DMR-1420570 (D.J.M.) from the National Science Foundation (NSF). The content is solely the responsibility of the authors and does not necessarily represent the official views of the National Institutes of Health or the NSF. S.L.M. acknowledges funding support from the National Institute of Arthritis and Musculoskeletal and Skin Diseases (F31AR075367). B.R.F. acknowledges funding support from the National Institutes of Health (F32 AG057135). I.d.L. acknowledges funding support from the National Cancer Institute (U01CA214369). **Author contributions:** B.R.S., C.J.P., C.J.W., and D.J.M. conceived and designed the research. B.R.S., S.L.M., B.R.F., S.N., B.J.K., I.d.L., M.D., J.T.A., and M.O.D. performed the experiments, C.J.P. designed and built the robotic device, and H.H.V. provided scientific and technical feedback on this work. B.R.S. and D.J.M. wrote the paper. All authors reviewed and commented on the manuscript. **Competing interests:** D.J.M. and C.J.W. are inventors on patent/patent application (U.S. Patent Application no. 15/776,853, publication no. US 2020/0222582) held/submitted by Harvard University/Wyss Institute for this study. The authors declare that they have no other competing interests. **Data and materials availability:** All data associated with this study are present in the paper or the Supplementary Materials.

Submitted 21 September 2020
Resubmitted 29 May 2021
Accepted 10 September 2021
Published 6 October 2021
10.1126/scitranslmed.abe8868

Citation: B. R. Seo, C. J. Payne, S. L. McNamara, B. R. Freedman, B. J. Kwee, S. Nam, I. de Lázaro, M. Darnell, J. T. Alvarez, M. O. Dellacherie, H. H. Vandenburgh, C. J. Walsh, D. J. Mooney, Skeletal muscle regeneration with robotic actuation–mediated clearance of neutrophils. *Sci. Transl. Med.* **13**, eabe8868 (2021).

Science Translational Medicine

Skeletal muscle regeneration with robotic actuation–mediated clearance of neutrophils

Bo Ri Seo, Christopher J. Payne, Stephanie L. McNamara, Benjamin R. Freedman, Brian J. Kwee, Sungmin Nam, Irene de Lzaro, Max Darnell, Jonathan T. Alvarez, Maxence O. Dellacherie, Herman H. Vandenburgh, Conor J. Walsh, and David J. Mooney

Sci. Transl. Med., **13** (614), eabe8868.
DOI: 10.1126/scitranslmed.abe8868

The mechanics of muscle regeneration

Immune cells play an important role in skeletal muscle response to injury. Seo *et al.* studied the effects of mechanical loading on hindlimb muscle regeneration after intramuscular myotoxin injection and ischemia in mice. Compressive force applied via a soft-interface robotic system facilitated neutrophil clearance, reduced proinflammatory cytokines and chemokines, and improved muscle fiber composition and function. Results support the development of therapeutic mechanical stimulation regimens to accelerate muscle regeneration.